A&A manuscript no.
(will be inserted by hand later)

Your thesaurus codes are:
08 (09.04.1; 09.13.2; 09.01.1; 13.09.4; 08.06.2; 10.01.1)

ASTRONOMY
AND
ASTROPHYSICS

arXiv:astro-ph/9909477v2 29 Jan 2000

ISO–SWS observations of interstellar solid $^{13}CO_2$: heated ice and the Galactic $^{12}C/^{13}C$ abundance ratio*

A.C.A. Boogert[1,2,3], **P. Ehrenfreund**[4], **P.A. Gerakines**[5,6], **A.G.G.M. Tielens**[1,2], **D.C.B. Whittet**[5], **W.A. Schutte**[4], **E.F. van Dishoeck**[4], **Th. de Graauw**[1,2], **L. Decin**[7], **and T. Prusti**[8]

[1] Kapteyn Astronomical Institute, P.O. Box 800, NL-9700 AV Groningen, the Netherlands
[2] SRON, P.O. Box 800, NL-9700 AV Groningen, the Netherlands
[3] Present address: California Institute of Technology, Downs Laboratory of Physics 320-47, Pasadena, CA 91125, USA
[4] Leiden Observatory, P. O. Box 9513, NL-2300 RA Leiden, the Netherlands
[5] Department of Physics, Applied Physics & Astronomy, Rensselaer Polytechnic Institute, Troy, NY 12180, USA
[6] Present address: Code 691, NASA/Goddard Space Flight Center, Greenbelt, MD 20771, USA
[7] Instituut voor Sterrenkunde, K.U. Leuven, Celestijnenlaan 200B, B-3001 Heverlee, Belgium
[8] ISO Data Centre, Astrophysics Division, ESA, Villafranca del Castillo, P.O. Box 50727, E-28080 Madrid, Spain

Received 29 July 1998/ Accepted 12 October 1999

Abstract. We present observations of the stretching mode of $^{13}CO_2$ ice along 13 lines of sight in the Galaxy, using the *Short Wavelength Spectrometer* on board of the *Infrared Space Observatory* (ISO–SWS). Remarkable variations are seen in the absorption band profile in the different lines of sight. The main feature is attributed to $^{13}CO_2$ mixed with polar molecules such as H_2O, and CH_3OH. The high-mass protostars GL 2136, GL 2591, S 140 : IRS1, and W 3 : IRS5 show an additional narrow substructure at 2282 cm^{-1} (4.382 μm), which we attribute to a polar, CH_3OH–containing CO_2 ice, that experienced heating. This heating effect is sustained by a good correlation of the strength of the substructure with dust and CO gas temperatures along the line of sight, and anti-correlation with ice abundances. Thus, our main conclusion is that interstellar CO_2 ices around luminous protostars are subjected to, and altered by, thermal processing and that it may reflect the evolutionary stage of the nearby protostar. In contrast, the ices around low mass protostars and in a quiescent cloud in our sample do not show signs of thermal processing.

Furthermore, we determine for the first time the Galactic $^{12}C/^{13}C$ ratio from the solid state as a function of Galacto-centric radius. The $^{12}CO_2/^{13}CO_2$ ratio for the local ISM (69±15), as well as the dependence on Galacto-centric radius, are in good agreement with gas phase ($C^{18}O$, H_2CO) studies. For the few individual objects for which gas phase values are available, the $^{12}C/^{13}C$ ratios derived from CO_2 tend to be higher compared to CO studies (albeit with $\sim 2.5\ \sigma$ significance only). We discuss the implications of this possible difference for the chemical origin of interstellar CO_2.

Key words: ISM: dust, extinction – molecules – abundances – Infrared: ISM:lines and bands – Galaxy: abundances – Stars: formation

1. Introduction

Space based observations have revealed that the CO_2 molecule is an important constituent of quiescent and star forming molecular clouds (d'Hendecourt & de Muizon 1989; de Graauw et al. 1996; d'Hendecourt et al. 1996; Gürtler et al. 1996; Strazzulla et al. 1998; Whittet et al. 1998; Gerakines et al. 1999). It is primarily present in the solid state (Van Dishoeck et al. 1996), with an abundance of typically 20% of water ice, consuming ∼3% of the carbon budget. The main focus of research has been on the high quality observations of the solid $^{12}CO_2$ stretching and bending modes at 4.27 and 15.2 μm, which are prominently present in the spectra obtained with ISO–SWS (Gerakines et al. 1999; Boogert 1999).

The detection of the $^{13}CO_2$ isotope, with a two orders of magnitude lower abundance, has been reported as well (de Graauw et al. 1996; d'Hendecourt et al. 1996). Its stretching mode frequency is well separated from that of $^{12}CO_2$ (4.38 μm vs. 4.27 μm). The analysis of this weak band is very attractive and has some specific advantages over $^{12}CO_2$ studies. It is an independent and very sensitive probe of the ice mantle composition. $^{13}CO_2$ is always a trace constituent. In contrast to $^{12}CO_2$, interactions of $^{13}CO_2$ molecules with themselves, and consequent effects

---

Send offprint requests to:
A.C.A. Boogert (boogert@submm.caltech.edu)

* Based on observations with ISO, an ESA project with instruments funded by ESA Member States (especially the PI countries: France, Germany, the Netherlands and the United Kingdom) and with the participation of ISAS and NASA.

on the band profile, are unimportant. For the same reason, the polarizability of the ice at the $^{13}CO_2$ resonance frequency can be neglected, and the absorption profile is insensitive to the shape and thickness of the ice mantle, and composition of the grain core, contrary to the $^{12}CO_2$ bands. Thus the laboratory spectrum can be compared directly to the interstellar spectrum, and uncertainties resulting from corrections induced by the grain shape or uncertain optical constants are avoided (Ehrenfreund et al. 1996; 1997).

The main motivation for our study is to determine the physical and chemical history of interstellar CO_2, and interstellar ices in general. Once interstellar ices are formed, by a combination of direct accretion from the gas phase and chemical reactions on grain surfaces, they can be exposed to a variety of violent processes. Among these are cosmic ray bombardment, ultraviolet irradiation, heating by visible and infrared photons, and disruption in shocks. What is the importance of these processes in various environments, such as protostars of low and high mass, and quiescent clouds? Can the ices around low mass protostars survive the various destruction mechanisms, and be included in comets? If so, how much do its composition and structure still resemble the interstellar ices? In order to answer these questions, we analyze the absorption band profile of the stretching mode of interstellar $^{13}CO_2$. We make use of a large database of spectra of CO_2 ices, with a range of compositions and temperatures, obtained in the Leiden Observatory Laboratory (Ehrenfreund et al. 1996; 1997; 1999). In a separate study, the analysis of the absorption bands of $^{12}CO_2$ will be presented (Gerakines et al. 1999).

Another important motivation for this study is to determine the $^{13}CO_2$ abundance, and derive the Galactic $^{12}C/^{13}C$ abundance ratio. It is the first time that the $^{12}C/^{13}C$ ratio is determined from the solid state. An important advantage over gas phase studies is that the column density can be straightforwardly derived from the observed integrated optical depth and the intrinsic band strength determined in the laboratory. In contrast, for gas phase species excitation, and radiative transfer models are required.

Previous (gas phase $C^{18}O$, H_2CO) studies have shown that the $^{12}C/^{13}C$ ratio increases with Galacto-centric radius, with $^{12}C/^{13}C$=25 in the Galactic Center, and $^{12}C/^{13}C$ = 77 in the local interstellar medium (see Wilson & Rood 1994 for an overview). Recent observations of atomic C and C^+ yield $^{12}C/^{13}C$=60 toward the Orion Bar (Keene et al. 1998). Determination of the $^{12}C/^{13}C$ ratio is an important input for evolutionary models of our Galaxy, since ^{12}C is produced by Helium burning by massive stars, which can be converted to ^{13}C in the CNO cycle of low- and intermediate-mass stars at later times.

Furthermore, comparison of the $^{12}C/^{13}C$ ratios derived from various species, will allow to determine the importance of chemical fractionation (^{13}C preferentially incorporated in CO) and isotope-selective destruction (^{13}CO preferentially destroyed). Models of photo-dissociation regions (PDRs), including chemical fractionation and isotope-selective destruction, show that the $^{12}C/^{13}C$ ratio for gaseous $C^{18}O$ can decrease by ∼50%. Recent observations of C and C^+, however, indicate that chemical fractionation is not an important effect, or is compensated for by isotope-selective photo dissociation, in these PDRs (Keene et al. 1998). We do not expect that these effects play an important role for the CO in our lines of sight, since they mainly trace dense molecular cloud material with low atomic C abundances. However, species that are formed from atomic C or C^+ rather than CO, may have very different $^{12}C/^{13}C$ ratios (e.g. H_2CO; Tielens 1997). Thus, the determination of the solid $^{12}CO_2/^{13}CO_2$ ratio is a potentially powerful tool to trace the chemical history of interstellar CO_2; does it originate from CO, as is generally assumed, or perhaps from $C^{(+)}$?

In Sect. 2 we present our ISO–SWS observations and data reduction techniques. The laboratory results of the $^{13}CO_2$ stretching mode are summarized in Sect. 3. The analysis of the interstellar $^{13}CO_2$ band profile, and derivation of the column densities is presented in Sect. 4. We discuss the main results in Sect. 5. First, we correlate the depth of the detected narrow 2282 cm^{-1} absorption feature with known physical parameters along the observed lines of sight. Then we compare the $^{12}C/^{13}C$ ratios, derived from solid CO_2 and gas phase molecules, and discuss the importance of chemical fractionation, and the reaction pathway to form CO_2. The summary and conclusions are given in Sect. 6.

2. Observations

The $^{13}CO_2$ spectra were obtained with ISO–SWS (de Graauw et al. 1996; Kessler et al. 1996). Most spectra were observed in the high resolution grating mode ($R = \lambda/\Delta\lambda$=1500; “SWS06” mode). Only the source GL 989 was observed in the fast scanning mode (“SWS01 speed 3”) at an effective resolving power R ∼400.

The spectra were reduced with version 6 of the SWS pipeline during January–April 1998 at SRON Groningen, using the latest calibration files available at that time. For some low flux spectra we applied a “pulse shape” correction on ERD level (de Graauw et al. 1996) to linearize the slopes, resulting in ∼10% better signal-to-noise. All detector scans were checked for excessive noise levels, deviating flux levels and continuum slopes, and dark current jumps. Bad scans were taken out off the data, and then the scans were “flat-fielded” to the median spectrum using a first order polynomial. Cosmic ray hits were removed by clipping all points deviating more than 3 σ from the median, and subsequently the scans were averaged and rebinned per scan direction to a resolving power of $R = 1500$ (R = 400 for GL 989). The effective ”signal-to-noise” values, as determined from the systematic differences be-

Table 1. Observed lines of sight

Object	RA (1950.0)	Dec (1950.0)	Revolution[a]	V^b_{helio} km s^{-1}	S/N[c]
W 3 : IRS5	02:21:53.1	+61:52:20	427	−43	65
Elias 16	04:36:34.4	+26:05:36	686	+16	65
NGC 2024 : IRS2	05:39:14.3	−01:55:59	667	+27	65
GL 989	06:38:25.3	+09:32:29	716	—[d]	100
Elias 29	16:24:07.7	−24:30:40	452	−7	100
GC 3	17:43:04.4	−28:48:27	327	—[e]	140
W 33A	18:11:44.2	−17:52:59	467	+20	65
GL 2136	18:19:36.6	−13:31:40	872	+13	100
R CrA : IRS2	18:58:19.0	−37:02:50	495	0.0	50
HH 100	18:58:28.2	−37:02:29	704	0.0	65
GL 2591	20:27:35.8	+40:01:14	357	−25	200
S 140 : IRS1	22:17:41.1	+63:03:42	263	−20	200
NGC 7538 : IRS9	23:11:52.8	+61:10:59	433	−70	100

[a] ISO revolution number
[b] Heliocentric velocity from literature
[c] Effective signal-to-noise of the $^{13}CO_2$ spectrum
[d] No radial velocity correction applied; spectrum has low resolution
[e] No radial velocity found in literature (see text)

tween the SWS up and down scans, are given in Table 1. We note that due to the weakness of the interstellar $^{13}CO_2$ band, ∼ 10% of the continuum, our analysis (column densities, band profiles) is not significantly affected by detector memory effects, known to exist at this wavelength. Also, the detector response function is very smooth over the narrow $^{13}CO_2$ band, and thus will not induce spurious features due to small wavelength calibration errors or dark current uncertainties.

An accurate wavelength calibration is important for our study. The standard SWS wavelength calibration was applied (Valentijn et al. 1996). The satellite velocity was converted to the heliocentric reference frame, using standard ISO–SWS pipeline routines. Then we corrected for the source velocity in the heliocentric frame, using published radial velocities for each source (Table 1). Recent millimeter observations of $C^{17}O$ emission lines show velocity shifts that are in excellent agreement with the values that we use (Van der Tak et al., in prep.). To check the accuracy of the wavelength calibration and velocity corrections, we compared the position of ro-vibrational ^{12}CO gas phase lines (^{13}CO lines are too weak), when present in the same spectrum, with peak positions from the HITRAN database (Rothman et al. 1992). For S 140 : IRS1, and W 3 : IRS5 the lines are blue-shifted by 10% of a resolution element (∼0.15 cm^{-1}; ∼20 km s^{-1}) compared to the HITRAN wavelengths, for GL 2591 by 20%, and for GL 2136 by 30%. Part of this blue-shift may be real. Mitchell et al. (1991) find that, whereas the velocity shift of ^{13}CO lines is in good agreement with millimeter studies, the ^{12}CO absorption lines show significant blue shifted shoulders and sub-peaks, originating from the outflow associated with the protostar. At the much lower resolution of our observations (∼160 km s^{-1}), this may result in a blue shift of the ^{12}CO absorption line. However, the main absorption is present at the cloud velocity, and at our resolution the peak would shift by not more than −15 km s^{-1} (GL 2591), −10 km s^{-1} (W 3 : IRS5) or much less than that for the other sources. Thus, we attribute the CO line shifts in the ISO–SWS spectra primarily to uncertainties in the wavelength calibration and small pointing errors. In particular, GL 2136 was observed at the end of the ISO mission for which no updated wavelength calibration files are available yet. We applied the small shift derived from the CO lines to further improve the wavelength calibration of the $^{13}CO_2$ band. For one object, GC 3, we found no radial velocity observation in the literature, and determined it from the CO lines to be $v_{\mathrm{helio}} = -90$ km s^{-1}. The fully reduced spectra are given in Fig. 1.

3. Laboratory CO_2 studies

The absorption band profiles of the stretching and bending modes of $^{12}CO_2$ and $^{13}CO_2$ in apolar ices (CO, N_2, O_2) were extensively studied in the laboratory by Ehrenfreund et al. (1996; 1997). Additional experiments of CO_2 mixed with polar molecules (H_2O, CH_3OH) were performed in the Leiden Observatory Laboratory as well (Ehrenfreund et al., 1998; 1999). Figure 2a summarizes the peak shifts and broadenings of the stretching mode of $^{13}CO_2$ in these ices at a temperature T =10 K.

For a pure CO_2 ice, i.e. $^{12}CO_2$:$^{13}CO_2$=90:1, the absorption band of $^{13}CO_2$ is centered on 2283.0 cm^{-1} and is

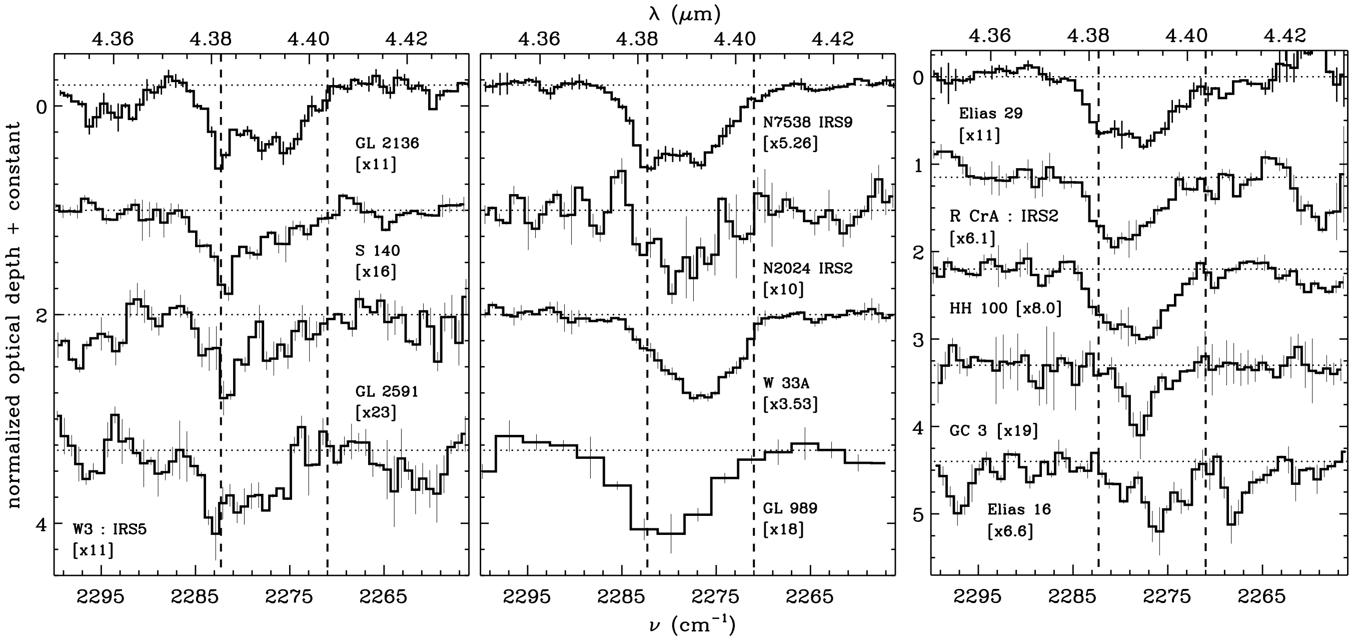

Fig. 1. The ISO–SWS spectra of $^{13}CO_2$ on optical depth scale toward massive protostars (left two panels). The right panel shows low-mass protostars, a background star of the Taurus Molecular Cloud (Elias 16) and a Galactic Center source (GC 3). The spectra were normalized to the peak optical depth by multiplication with the factors given in square brackets. The error bars were determined from the difference between the ISO–SWS up and down scans, and thus include systematic errors. The vertical dashed lines are given to facilitate comparison of the spectra in the different panels.

very narrow (FWHM$\sim$2.3 cm^{-1}). A large broadening and shift to lower frequencies is observed when H_2O is added. An even larger peak shift, up to 2274 cm^{-1}, but a small narrowing, occurs in CO_2:CH_3OH ices. This difference in spectroscopic behavior of H_2O:CO_2 and CH_3OH:CO_2 ices is also particularly evident in the $^{12}CO_2$ bending mode (Ehrenfreund et al. 1998; 1999). It is ascribed to the formation of stable $CH_3OH.CO_2$ complexes. Thus, at low temperatures, H_2O and CH_3OH–rich CO_2 ices have very distinct $^{13}CO_2$ peak positions. Mixtures of CO_2 with both H_2O and CH_3OH lie in between these extremes, as indicated by the "weak" (H_2O:CH_3OH:CO_2=7:0.6:1) and "strong" (H_2O: CH_3OH: CO_2=1.7:0.6:1) interstellar mixtures in Fig. 2a. Apolar molecules, such as CO and O_2, induce much smaller broadenings and peak shifts to the $^{13}CO_2$ ice band. Thus, the laboratory simulations show that the $^{13}CO_2$ stretching mode is a sensitive probe to discriminate between interstellar polar and apolar ices.

The peak position and width depend strongly on the temperature of the ice. Upon warm-up, the peak position of $^{13}CO_2$ in H_2O–, and CH_3OH–rich ices (with less than $\sim$20% of CO_2) shifts significantly to lower frequencies, and at the same time becomes narrower (Fig. 2b). For example, in the mixture H_2O:CO_2=10:1, the $^{13}CO_2$ band shifts by 2.5 cm^{-1}, and the FWHM decreases with 2.5 cm^{-1}, when heated from T =10 to 140 K in the laboratory. Unfortunately, heating of the polar, CO_2–poor ice has the same effect on the band profile as increasing the H_2O/CO_2 and CH_3OH/CO_2 mixing ratios (Figs. 2a and 2b). Thus, the $^{13}CO_2$ stretching mode is less suited to determine an accurate $H_2O/CH_3OH/CO_2$ mixing ratio, or the precise temperature of these particular ices. However, for H_2O:CO_2 and CH_3OH:CO_2 ices with CO_2 concentrations between 20-90%, heating induces a very specific spectroscopic signature. The $^{13}CO_2$ profile becomes asymmetric at a laboratory temperature of T $\sim$50 K, and $\sim$105 K respectively (Figs. 2 and 3; see Sect. 5.1 for the corresponding temperatures in interstellar space). A second peak develops at the blue side of the band, which is reflected in Fig. 2b as a "broadening" of the overall profile. At higher temperatures, this new peak dominates the $^{13}CO_2$ spectrum. Its peak position of $\sim$2282–2283 cm^{-1}, and narrow width ($\sim$3 cm^{-1}) are close to the values for a pure CO_2 ice, although, in particular for CH_3OH ices, this correspondence is not exact. This spectroscopic behavior is attributed to the destruction of bonds between the polar molecules and CO_2, and the formation of new, stronger, hydrogen bonds between the polar molecules (Ehrenfreund et al. 1999). The CO_2 molecules now interact primarily with themselves. This re-arrangement of bonds ("segregation") is also particularly well traced in the $^{12}CO_2$ bending mode, which shows, after heating, the typical double peaked structure of a pure CO_2 ice (Ehrenfreund et al., 1999). In accordance with heating experi-

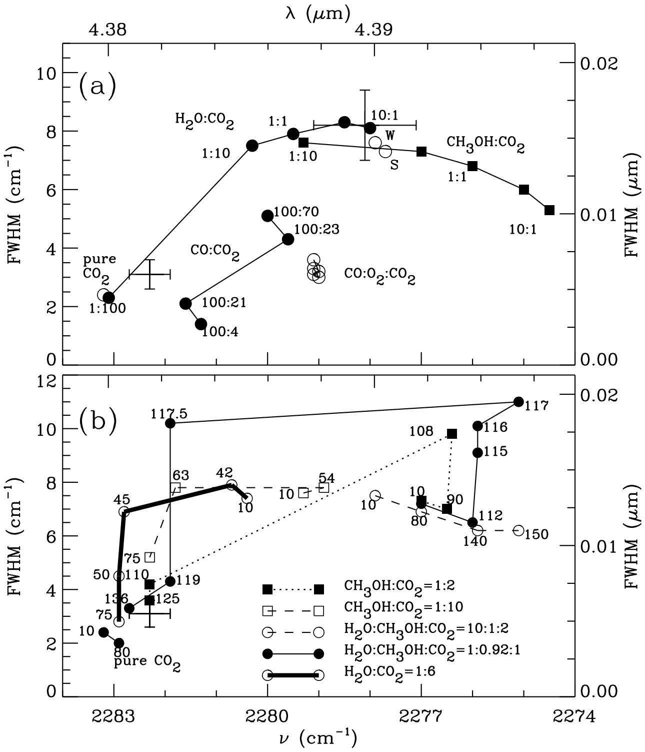

Fig. 2. a and b. Laboratory spectroscopy of the stretching mode of $^{13}CO_2$ ice at T =10 K (**a**), and at higher temperatures (**b**). The average Gaussian parameters of the interstellar spectra are given by crosses. In panel **a**, the peak position versus width variations are shown for CO_2 in series of increasing H_2O, CH_3OH, and CO abundances (connected with a line). "W" and "S" indicate the weak and strong interstellar mixtures (see text). Panel **b** clearly illustrates the large effect of temperature on width and peak position of the $^{13}CO_2$ stretching mode, due to the segregation of CO_2.

ments of H_2O:CH_3OH ices (Blake et al. 1991), it seems likely that also a spatial segregation exists between the CO_2 molecules and polar species. Crystalline phases of H_2O ice enclosing 0.1 μm size pockets of CH_3OH were observed in these heated H_2O:CH_3OH ices. Such microscopic observations are essential to determine the structure of heated polar CO_2 ices as well.

Finally, for apolar ices containing CO, O_2, and N_2, the $^{13}CO_2$ band shifts to higher frequencies, and becomes narrower upon warm-up. This can be attributed to evaporation of the host molecule. These laboratory results will be used to derive the composition of interstellar ice, i.e. polar versus apolar, and possibly its temperature history.

4. Results

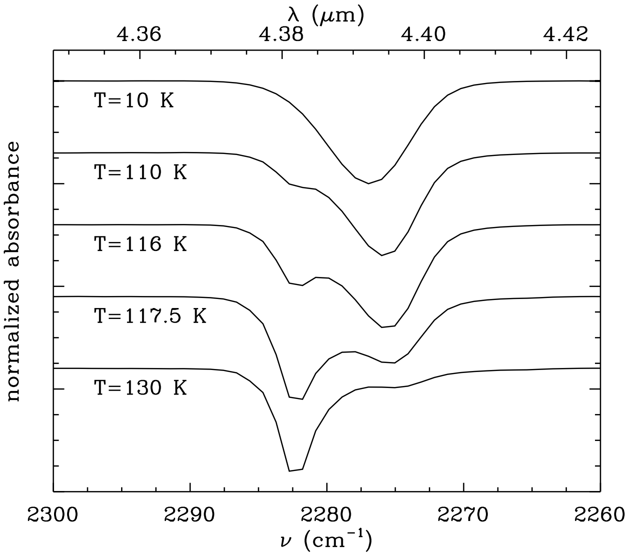

Fig. 3. Effect of heating on the $^{13}CO_2$ stretching mode in the ice mixture H_2O:CH_3OH:CO_2=1:0.92:1. This shows clearly the segregation of CO_2 at high temperatures. The peak at ∼2282 cm^{-1} is close to the peak position for a pure CO_2 ice (Fig. 2). We note that the indicated temperature was measured in the laboratory. At the much longer time scales in interstellar space, the segregation temperature is much lower (∼78 K; Sect. 5.1).

4.1. Contamination by gas phase lines

The spectral region of the $^{13}CO_2$ ice band is contaminated by narrow absorption lines of gas phase CO in the lines of sight of GL 2136, GL 2591, and possibly S 140 : IRS1 (Fig. 4). They originate from CO in the ground vibrational state (v=0–1), at high rotational levels, up to perhaps J=45. The presence of hot CO gas in these lines of sight was shown in other studies as well (e.g. Mitchell et al. 1990; Table 4). The main component of the $^{13}CO_2$ ice band is much broader than the unresolved gas phase CO lines, and our conclusions are not influenced by this contamination. However, the narrow line at 2282 cm^{-1} detected in these sources (Sect. 4.2) is at the same frequency as the CO J=46→47 R-branch line. It is unlikely that this line can be attributed to gaseous CO, given its large depth relative to neighboring R-branch lines, in particular for S 140 : IRS1. Furthermore, we checked for the presence of features from vibrationally excited ^{12}CO. The band head of the v=1–2 transition at ∼2298 cm^{-1} (Goorvitch 1994) may be present toward GL 2136, and GL 2591 (Fig. 4). This feature is well separated from the $^{13}CO_2$ ice band. There is no indication for absorption at the frequency of the v=2–3 band head (∼2268 cm^{-1}). Given the weakness of these ^{12}CO band heads, the contribution of the v=0–1 band head of ^{13}CO (∼2276 cm^{-1}) to the $^{13}CO_2$ ice band can probably be neglected.

One object in our sample, Elias 16, is an evolved star located behind the Taurus molecular cloud. It is a K 1 giant (Elias 1978), and the 2–5 μm spectral region shows many narrow absorption lines, most likely associated with the photosphere of this object (Whittet et al. 1998). In the spectral region for this study (~2260–2300 cm^{-1}), we detect narrow absorption lines at 2268, and 2297 cm^{-1} (Fig. 1). These lines are well separated from the region where $^{13}CO_2$ ice absorption is expected, and are attributed to the v=2–3 and v=1–2 band heads of ^{12}CO (Goorvitch 1994). However, another narrow line at 2276 cm^{-1}, probably the v=0–1 band head of ^{13}CO, might be blended with the $^{13}CO_2$ feature. We compared the spectrum of Elias 16 with the K 1.5 giant α Bootis (Fig. 5). The spectral type of these stars is very similar, and indeed α Bootis does show absorption lines at 2268, 2276, and 2297 cm^{-1}. However, the lines in α Bootis have rather prominent wings on the red side, which are not recognized in Elias 16. Perhaps the spectral type or luminosity class of Elias 16 deviates from a K 1 giant. To correct for photospheric absorption, we subtracted the optical depth spectrum of α Bootis from Elias 16 (Fig. 5). The narrow lines at 2268, and 2297 cm^{-1} are nicely removed, giving confidence in the correctness of this method. A significant absorption remains at ~2278 cm^{-1}, which we attribute to solid $^{13}CO_2$ in the Taurus molecular cloud. In our further analysis, we used this corrected spectrum of Elias 16.

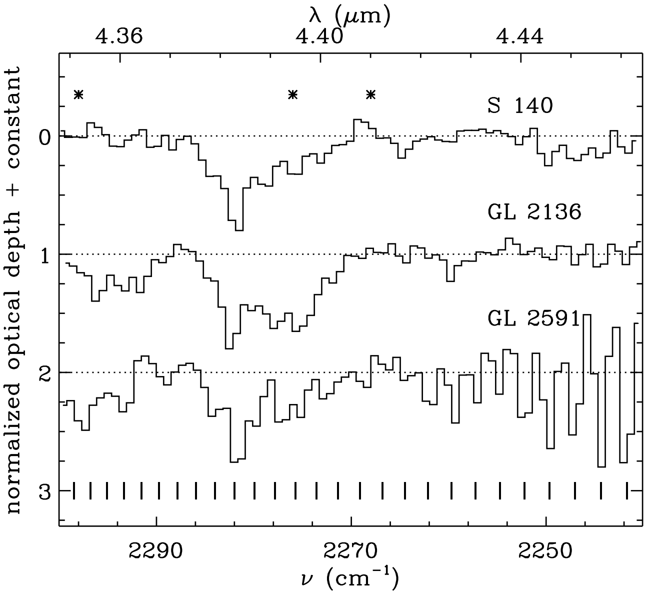

Fig. 4. Comparison of gas phase CO frequencies with sources showing fine structure. The thick vertical lines indicate the frequency of the R-branch lines of gaseous CO, originating from rotational levels $J = 29$ (2241.7 cm^{-1}) to $J = 53$ (2295.1 cm^{-1}) in the lowest vibrational state (v=0–1). The $*$ symbols on top indicate the expected frequencies of the CO band heads (see text). We attribute the sharp feature at 2282 cm^{-1} and the underlying broader component to interstellar solid $^{13}CO_2$.

4.2. Interstellar solid $^{13}CO_2$ band profile analysis

The $^{13}CO_2$ band profile varies remarkably between the observed lines of sight (Fig. 1). Two independent components are present. The high-mass protostars GL 2136, S 140 : IRS1, W 3 : IRS5, and GL 2591 show both a "broad" absorption extending over 2270–2287 cm^{-1}, and a very narrow feature at ~2282 cm^{-1}. Two lines of sight do not show the narrow component (Elias 16, GC 3), while in others it may be blended with the blue edge of the broader feature. In NGC 2024 : IRS2 and GC 3 the profile analysis is limited by a low depth and poor signal-to-noise, while in GL 989 the resolving power is too low to resolve the narrow feature, if present.

We followed two different approaches to analyze the interstellar $^{13}CO_2$ band profile. First, analogous to the solid CO band (e.g. Tielens et al. 1991), the narrow and broad component may originate from different ices along the line of sight. The ice composition and structure depend on the chemical (e.g. the H/CO ratio) and physical (e.g. temperature) history, which may have varied along the line of sight. Therefore, we decomposed the absorption band by fitting Gaussians to the observed broad and narrow components, and we compared the peak positions and widths with the laboratory results (Figs. 2, and 6). In our second approach, we investigate whether the $^{13}CO_2$ ice band profile can be explained by a single ice. Here, we determine the observed peak position and width (not fitting Gaussians) and again compare these with the laboratory results in Figs. 2, and 6. Both methods provide good insight in the characteristics of the observed band profile, and the variations between the various lines of sight.

4.2.1. Two component ices

For five objects in our sample, good fits are obtained by fitting two Gaussians: NGC 7538 : IRS9, GL 2136, S 140 : IRS1, GL 2591, and W 3 : IRS5 (Table 2). For the other lines of sight, no significant improvement is achieved, when using two instead of one Gaussian. Nevertheless, for some sources the narrow 2282 cm^{-1} feature might be blended with the blue edge of the broader component, and we do perform a fit with two Gaussians as well.

For the broad component we find a Gaussian FWHM of typically 6-9 cm^{-1}, with a peak position varying between 2276–2280 cm^{-1} for the different objects. Thus, this feature can be ascribed to absorption by $^{13}CO_2$ ice mixed with molecules with a large dipole moment, i.e. H_2O and CH_3OH (Figs. 2 and 6b; Table 2). To derive the chemical history of interstellar CO_2 it is important to determine the relative amounts of H_2O, CH_3OH, and CO_2 mixed in the ice. At high CH_3OH concentrations, both CH_3OH:CO_2 and H_2O:CH_3OH:CO_2 laboratory ices have a $^{13}CO_2$ band

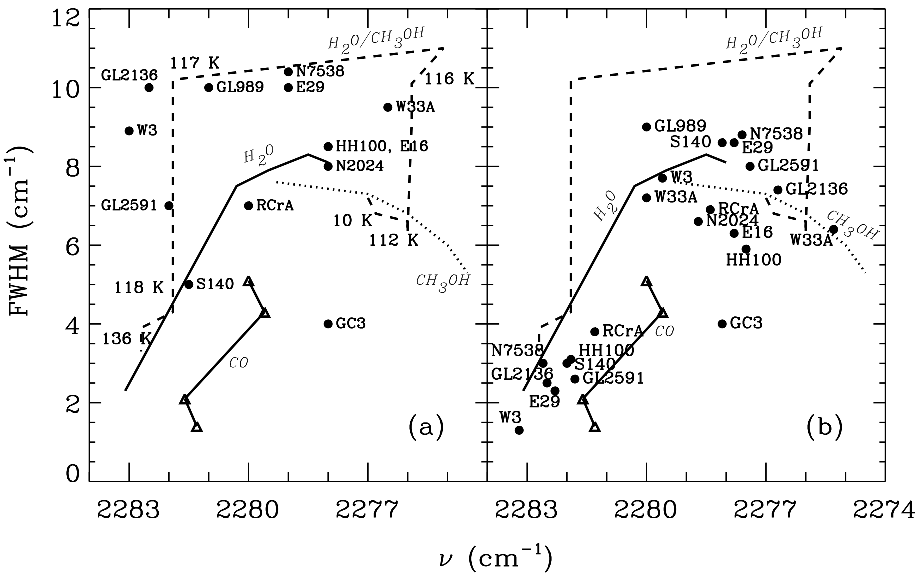

Fig. 6. **a** Observed peak position and FWHM of solid $^{13}CO_2$ for all observed sources. The lines represent the peak and FWHM of the laboratory experiments as presented in Fig. 2. The dashed line is the mixture H_2O:CH_3OH:CO_2=1:0.92:1 at the indicated temperatures. **b** Same as panel **(a)**, but here the observed interstellar $^{13}CO_2$ band is decomposed with Gaussians. This Figure shows that most interstellar $^{13}CO_2$ bands can be explained by a single mixture at different temperatures **(a)** or by a strongly heated "segregated" ice component together with a non-segregated (perhaps cold) component **(b)**.

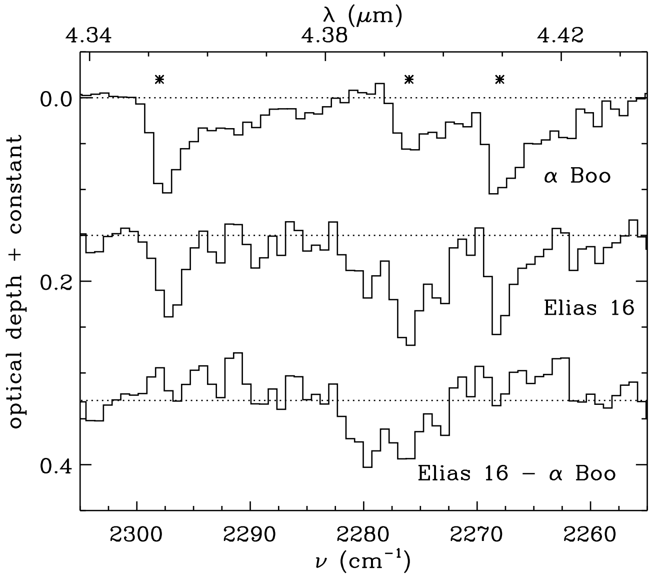

Fig. 5. Comparison of the spectra of Elias 16 and the K giant α Bootis on optical depth scale. The bottom spectrum is the subtraction of α Bootis from Elias 16, to correct for photospheric lines. The $*$ symbols on top indicate the expected frequencies of the gas phase CO band heads (see text). The residual feature at $\sim$2278 cm^{-1} is attributed to $^{13}CO_2$ ice in the Taurus molecular cloud.

that peaks at frequencies less than $\sim$2276.0 cm^{-1}. Thus, we can exclude that the ice is CH_3OH-rich, i.e. we conclude that $CH_3OH/CO_2 \leq 1$, which is in good agreement with the observed column densities (Sect. 4.4).

For several reasons, the broad component of the $^{13}CO_2$ absorption band does not provide further constraints on the CH_3OH/CO_2 mixing ratio, nor the H_2O/CO_2 ratio. First, although the width of the absorption band is a good discriminator between polar and and apolar ices (Sect. 3), it depends only weakly on the relative abundance of H_2O and CH_3OH in the ice (Fig. 2). Second, for peak positions in the range 2277.5-2279.5 cm^{-1} there is an ambiguity between H_2O, and CH_3OH ices. Good fits to the interstellar spectra can be obtained with H_2O:CO_2, CH_3OH:CO_2, as well as H_2O:CH_3OH:CO_2 ices at a range of temperatures. Thus, although we can put an upper limit of $CH_3OH/CO_2 \leq 1$, no lower limit to the CH_3OH concentration can be set from the broad $^{13}CO_2$ component. Furthermore, for most objects good fits are obtained for a wide range of H_2O concentrations. In some lines of sight we can put a significant lower limit $H_2O/CO_2 \geq 1$, when fitting H_2O:CO_2 ices (e.g. Elias 29, NGC 7538 : IRS9, W 33A). However, when adding CH_3OH to the ice, equally good fits with even lower H_2O concentrations can be obtained.

The peak position of the narrow component is remarkably constant with a weighted mean of 2282.5±0.2 cm^{-1}, while the width is typically FWHM=2.5 cm^{-1}. This small width can be ascribed to $^{13}CO_2$ interacting with apolar molecules (Figs. 2 and 6b). The accurate peak position provides further constraints to the origin of this feature. For some sources (GL 2136, W 3 : IRS5), both pure CO_2 and heated "segregated" polar CO_2 ices provide good fits. However, for the sources with the strongest narrow peaks (S 140 : IRS1, and GL 2591), the best fits are only obtained by heated polar CO_2 ices, showing segregation behavior. These ices must contain CH_3OH, and may contain H_2O (but not necessarily). The initial CO_2 concentration in these heated CH_3OH–containing ices must be in between 20-90%. At higher CO_2 concentrations, the peak position and width are not well matched (Fig. 7). At very low CO_2 concentrations, no segregation takes place upon heating (see Sect. 3 and the CH_3OH:CO_2=1:10 ice in Fig. 2).

Table 2. The observed peak position (ν), width (FWHM), and peak optical depth (τ) of the interstellar solid $^{13}CO_2$ band. For sources with high quality spectra we give in each second line the results of a decomposition of the profile, using 2 Gaussians. The standard deviation σ is given in parentheses.

Object	ν cm^{-1}	FWHM cm^{-1}	τ	ν cm^{-1}	FWHM cm^{-1}	τ
S 140 : IRS1	2281.5 (0.8)	5 (3)	0.050 (0.005)	-	-	-
	2278.1 (1.8)	9 (3)	0.021 (0.003)	2282.0 (0.6)	3.0 (1.5)	0.034 (0.002)
GL 2591	2282.0 (0.8)	7 (3)	0.034 (0.005)	-	-	-
	2277.4 (1.5)	8 (3)	0.015 (0.002)	2281.8 (0.3)	2.6 (1.2)	0.028 (0.003)
GL 2136	2282.5 (0.8)	10 (1)	0.071 (0.008)	-	-	-
	2276.7 (0.5)	7 (1)	0.056 (0.004)	2282.5 (0.5)	2.5 (0.6)	0.055 (0.003)
W 3 : IRS5	2283.0 (0.8)	8.9 (0.8)	0.073 (0.012)	-	-	-
	2279.6 (0.8)	8 (2)	0.050 (0.008)	2283.2 (0.3)	1.3 (0.7)	0.049 (0.005)
NGC 7538 : IRS9	2279.0 (2.0)	10.4 (0.8)	0.15 (0.01)	-	-	-
	2277.6 (0.2)	8.8 (0.4)	0.138 (0.004)	2282.6 (0.2)	3.0 (0.4)	0.091 (0.003)
Elias 29^{a}	2279.0 (2.0)	10 (1.5)	0.071 (0.009)	-	-	-
	2277.8 (1.2)	8.6 (2.3)	0.064 (0.004)	2282.3 (1.4)	2.3 (2.9)	0.026 (0.005)
W 33A^{a}	2276.5 (1.0)	9.5 (0.8)	0.225 (0.015)	-	-	-
	2275.3 (0.2)	6.4 (0.4)	0.177 (0.008)	2280.0 (0.4)	7.2 (0.7)	0.119 (0.008)
Elias 16	2278.0 (2.0)	8.5 (1.5)	0.060 (0.017)	-	-	-
GC 3	2278.0 (0.8)	4 (2)	0.042 (0.015)	-	-	-
R CrA : IRS2^{a}	2280.0 (1.0)	7 (1)	0.13 (0.02)	-	-	-
	2278.4 (0.6)	6.9 (1.1)	0.092 (0.008)	2281.3 (0.6)	3.8 (1.2)	0.064 (0.005)
NGC 2024 : IRS2	2278 (2)	8 (2)	0.060 (0.015)	-	-	-
HH 100^{a}	2278 (2)	8.5 (1.0)	0.100 (0.015)	-	-	-
	2277.5 (0.4)	5.9 (0.7)	0.098 (0.008)	2281.9 (0.5)	3.1 (1.0)	0.053 (0.005)
GL 989^{b}	2281 (2)	10 (3)	0.046 (0.008)	-	-	-

[a] Equally good fits are obtained with 1 and 2 Gaussians (see text).

[b] Moderate spectral resolution; narrow component unresolved.

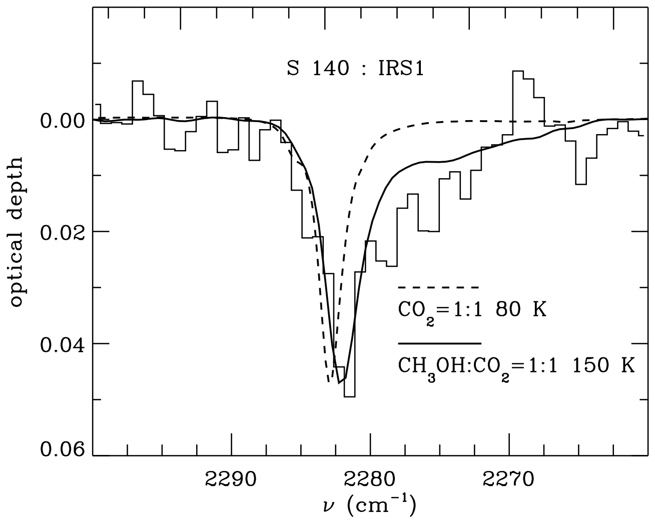

Fig. 7. Laboratory fits to the narrow $^{13}CO_2$ component of S 140 : IRS1, indicating that a heated "segregated" CH_3OH containing ice, rather than a pure CO_2 ice is needed to fit the exact peak position.

For completeness, we mention that satisfactory fits to the narrow features in GL 2591, and S 140 : IRS1 are also obtained by CO-rich ices, peaking at 2281.7 cm^{-1}. However, in these lines of sight no CO ice was detected (van Dishoeck et al. 1996; Gerakines et al. 1999; Table 4), and these mixtures can be excluded.

Concluding, the detected narrow 2282 cm^{-1} component can be well fitted with a heated polar CO_2 ice showing segregation. For at least two sources in our sample, this ice must contain CH_3OH ($CH_3OH/CO_2>0.10$) to fit the exact peak position. For the other sources, a pure CO_2 gives reasonable fits as well, but mixtures with significant amounts of other apolar species (CO, O_2) can be excluded.

4.2.2. Single component ices

When comparing the observed peak frequencies and overall widths (not fitting Gaussians) with the laboratory results, we find that toward most lines of sight the complete $^{13}CO_2$ ice band profile can be fitted with one single ice at a specific laboratory temperature (Figs. 6a and 8). Good fits are obtained with an ice in which H_2O, CH_3OH, and CO_2 are about equally abundant, which is in good agreement with studies of the $^{12}CO_2$ bending mode (Gerakines et al. 1999). However, equally good fits are obtained with other mixing ratios as well. For objects showing evidence for a separate 2282 cm^{-1} component (e.g. S 140, GL 2591), the ice must contain at least some CH_3OH to fit the peak position (CH_3OH/CO_2>0.10) and the H_2O abundance must not be too large (H_2O/CO_2<3). To fit W 33A with a single ice, the CH_3OH abundance must be at least 30% of CO_2. In contrast, the object R CrA : IRS2 must have an CH_3OH/CO_2 ratio less than ∼50% (note the offset from the other sources in Fig. 6a). For other objects, such as HH 100, the ice composition can not be significantly constrained.

If we do assume that the $^{13}CO_2$ band profile originates from a single ice, and it contains CH_3OH and H_2O with comparable concentrations, the temperatures of the best fitting laboratory spectra to the sources showing the 2282 cm^{-1} substructure are well constrained within the range $T = 115 - 118$ K (Figs. 6, and 8; Gerakines et al. 1999). At the long time scales in interstellar space, the segregation takes place at a much lower temperature of ∼77 K (Sect. 5.1).

4.3. CO_2 *column densities*

Column densities of solid $^{13}CO_2$ are given in Table 3 and were derived by integrating the optical depth in the frequency range 2269–2288 cm^{-1} and dividing this by the integrated band strength $A(^{13}CO_2)$. Laboratory experiments indicate that $A(^{13}CO_2)$ depends on the ice composition, but only weakly on temperature (Gerakines et al. 1995). The band strength is 7.8 10^{-17} cm $molecule^{-1}$ for pure CO_2 ice, and similar for the mixture H_2O:CO_2=1.6:1, but 15% lower for H_2O:CO_2=24:1. Since in the interstellar medium typically H_2O/CO_2< 5 (Sect. 4.4), we take $A(^{13}CO_2)$=7.8 10^{-17} cm $molecule^{-1}$. Note that the variation of $A(^{13}CO_2)$ seen in apolar CO and O_2 containing ices (Gerakines et al. 1995) is not applicable, since our study shows that interstellar CO_2 is absent in these ices. The error bars were determined from the average signal-to-noise values given in Table 1.

Using these $^{13}CO_2$ column densities, we are for the first time able to calculate the $^{12}CO_2/^{13}CO_2$ abundance ratio from the solid state, in a large number of sight-lines. The $^{12}CO_2$ column densities were derived from the $^{12}CO_2$ bending and stretching modes (∼4.27 and 15.2 μm; Gerakines et al. 1999). The column densities derived from both modes agree very well within the error bars given in Gerakines et al. (1999). These errors include ISO–SWS calibration uncertainties (mainly applicable to the stretching mode) and uncertainties due to the continuum determination, which is particularly difficult for the $^{12}CO_2$ bending mode, since it is blended with the bending mode of silicates (Gerakines et al. 1999; Boogert 1999).

The $^{12}CO_2/^{13}CO_2$ column density ratio has a relative error less than 16% in 6 lines of sight (Table 3). However, laboratory experiments have shown that the $^{12}CO_2/^{13}CO_2$ ratio can not be determined with an ac-

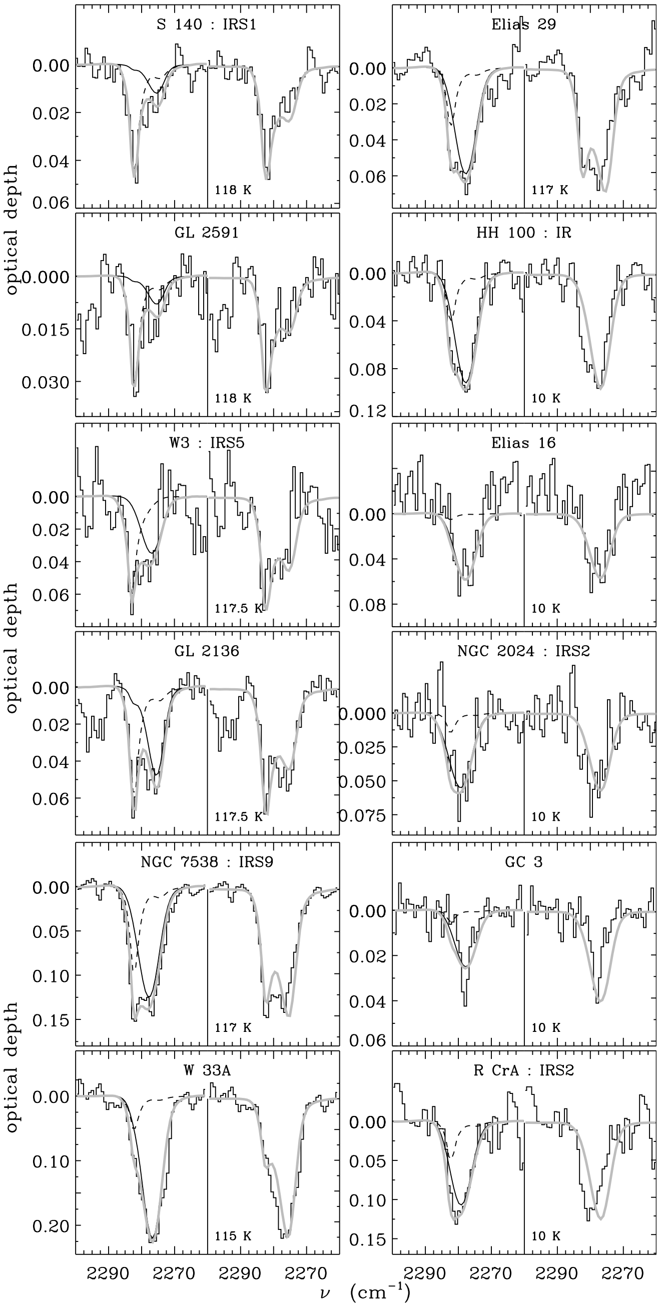

Fig. 8. Laboratory fits to the interstellar $^{13}CO_2$ band. For each source, the left panel gives a two component fit with the thin solid line representing a mixture of CO_2 with H_2O or CH_3OH. The dashed line is the mixture H_2O:CH_3OH:CO_2=1:1:1, heated to T =125 K. Note the significant variations in the relative contribution of these components. The thick gray line is the sum of both laboratory spectra. The right panel shows for each source the best fit with H_2O:CH_3OH:CO_2=1:0.92:1 at the indicated temperature. For sources that do not give good fits (e.g. HH 100), changing the mixing ratio somewhat will improve the fit at the indicated temperature. The luminous protostars in the left panels are ordered with a decreasing strength of the narrow 2282 cm^{-1} peak.

Table 3. The $^{13}CO_2$ column density and the $^{12}C/^{13}C$ ratio derived from solid CO_2 and gas phase CO.

Object	$N(^{13}CO_2)$	$^{12}C/^{13}C$		R_G^f
	10^{16}cm^{-2}	CO_2	CO^b	kpc
GC 3	0.21 (0.04)	52 (11)	24 (1)^c	0.5
W 33A	2.74 (0.21)	53 (8)	39 (1)^d	4.5
GL 2136	0.73 (0.05)	107 (8)		6.1
Elias 29	0.83 (0.05)	81 (11)		7.8
R CrA : IRS2	1.17 (0.09)	73 (16)		7.9
HH 100	1.03 (0.08)	52 (11)		7.9
GL 2591	0.26 (0.03)	62 (10)		7.9
Elias 16^a	0.47 (0.15)	98 (38)		8.2
S 140 : IRS1	0.38 (0.03)	111 (9)		8.4
NGC 2024 : IRS2	0.55 (0.13)	105 (33)		8.4
GL 989	0.62 (0.09)	84 (21)	62 (3)	8.7
NGC 7538 : IRS9	2.03 (0.12)	80 (11)		9.4
W 3 : IRS5	0.63 (0.13)	113 (37)	66 (4)^e	9.7

[a] $^{13}CO_2$ band corrected for photospheric OH absorption lines

[b] taken from Langer & Penzias (1990)

[c] Sgr B2, at (ΔRA, ΔDec)=(14.7', 26.1') from GC 3

[d] W 33(0,0), at (ΔRA, ΔDec)=(−6.0', −3.8') from W 33A

[e] W 3(OH), at (ΔRA, ΔDec)=(10.5', −13.3') from W 3 : IRS5

[f] galacto-centric radius calculated from Galactic coordinates from Simbad database and distances mentioned in Aitken et al. 1993 (GL 989, GL 2136, W 3 : IRS5), Chernin 1996 (NGC 2024 : IRS2), Gürtler et al. 1991 (GL 2591, S 140, NGC 7538 : IRS9, W 33A), Whittet 1974 (Elias 29), Saraceno et al. 1996 (HH 100, R CrA : IRS2, Elias 16), Okuda et al. 1990 (GC 3).

curacy better than 20% (Sandford & Allamandola 1990; Ehrenfreund et al. 1997), unless the ice composition is accurately known. The $^{12}CO_2/^{13}CO_2$ ratio of integrated optical depths is 19% lower in an H_2O:CO_2=1:10 ice compared to pure CO_2, and 14% higher for H_2O: CO_2= 5:1. For 3 objects with low statistical errors (GL 2136, GL 2591, and S 140), we find that the CO_2 is heated and segregated, closely resembling the band profile of pure CO_2. Thus, the band strengths are likely similar to pure CO_2. However, for Elias 29, W 33A, and NGC 7538 : IRS9 we can not exclude that a large fraction of the CO_2 is embedded in an H_2O-rich ice, and we conservatively assume a 14% error in the $^{12}CO_2/^{13}CO_2$ column density ratio for these sources.

Interesting variations in the $^{12}CO_2/^{13}CO_2$ ratio are evident. Most objects have ratios in between 70-110, but some are significantly lower, e.g. W 33A, GC 3 and HH 100. We will discuss these results in Sect. 5.3.

4.4. Further constraints on the solid H_2O/CO_2 *and* CH_3OH/CO_2 *ratios*

The composition of interstellar CO_2 ices can be further constrained by the CH_3OH, H_2O, and CO_2 column densities along the observed lines of sight. The H_2O/CO_2 ice column density ratio is typically ~ 5, but can be as high as 8 (GL 2136, GL 2591) and as low as 1.5 (GC 3; Gerakines et al. 1999). Thus, although mixtures with $H_2O/CO_2 \geq 10$ do provide good fits to most of the observed sources (e.g. W 33A, R CrA : IRS2), these mixtures are unrealistic. Furthermore, observations of the C–H stretching mode of CH_3OH (3.54 μm) indicate that $CH_3OH/H_2O \leq 0.10$ (Allamandola et al. 1992; Chiar et al. 1996), resulting in typically $CH_3OH/CO_2 \leq 0.50$. For some individual sources, the observed CH_3OH/CO_2 ratio is higher (W 33A: $CH_3OH/CO_2 = 1.90$), or lower (Elias 16: $CH_3OH/CO_2 < 0.20$). This is consistent with our conclusion that the interstellar $^{13}CO_2$ ice band for most sources is best fitted with laboratory ices with a low CH_3OH concentration, i.e. for which $0.1 < CH_3OH/CO_2 \leq 1$. To further limit the CH_3OH/CO_2 ratio in the ice, it is, in particular for the low mass protostars, important to obtain very sensitive observations of the C–H stretching mode of CH_3OH.

5. Discussion

5.1. Heating of CO_2 *ices*

The $^{13}CO_2$ ice band profile varies remarkably between the observed lines of sight. Most significant is the detection of a narrow substructure at $\sim$2282 cm^{-1} toward the massive protostellar objects S 140 : IRS1, GL 2136, GL 2591, and W 3 : IRS5. None of the low-mass protostars show this component, nor do some high-mass objects (W 33A, NGC 2024 : IRS2), the Galactic Center object GC 3, and quiescent cloud material traced by Elias 16. Laboratory simulations indicate that this distinct profile can be attributed to a heated, "segregated" polar CO_2 ice. Here, we further investigate this hypothesis by comparing the strength of the narrow $^{13}CO_2$ peak, normalized to the Gaussian depth of the broad component, to a number of established temperature tracers (Table 4).

Although only sources with a bolometric luminosity $L_{\rm bol} > 10^4\ L_\odot$ have detected narrow $^{13}CO_2$ peaks (Table 4; Fig. 9), a high luminosity can not be the only necessary condition. There is no, or very weak, sign of the $^{13}CO_2$ substructure in the luminous objects W 33A and NGC 7538 : IRS9. The dust temperature in these sight lines may be too low to cause the ice to segregate. The interstellar CO_2 ice affected by segregation must have a temperature of $T = 50-90$ K (or $\sim$100–180 K in the laboratory), depending on whether the ice is H_2O, or CH_3OH–rich. Assuming the dust radiates as a blackbody, modified by a power law emissivity with index -1, this corresponds to emission peaking at wavelengths of $\sim$25-50 μm. Non-heated ice, at temperatures of $\sim$20 K, radiates near

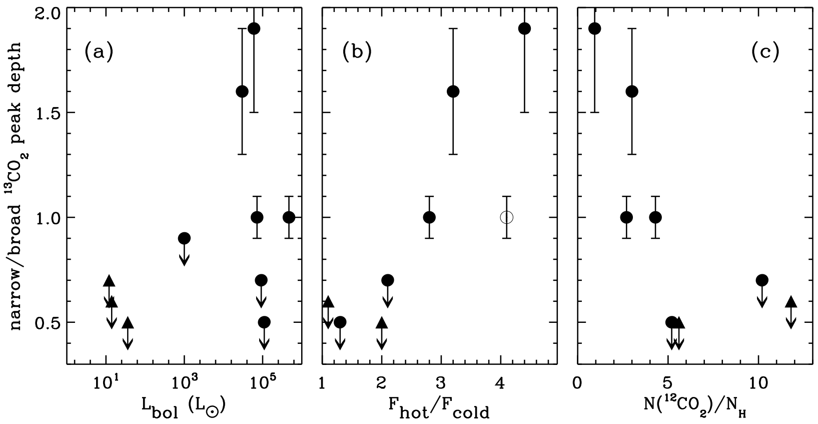

Fig. 9. a–c The strength of the narrow $^{13}CO_2$ peak plotted against various physical parameters of the protostars. High and low luminosity objects are indicated by bullets and triangles respectively. Panel **a** plots the bolometric luminosity, showing a poor correlation. The ratio of hot over cold dust emission in panel **b** gives a much better correlation. The far infrared flux ratio for W 3 : IRS5, indicated with an open symbol, is unreliable due to contamination in the large beam. Panel **c** shows that there is also a fairly good anti-correlation with the solid CO_2 abundance.

100 μm. Hence, a useful parameter for comparison is the flux ratio

$$\frac{F_{\rm hot}}{F_{\rm cold}} = \frac{F(45\ \mu{\rm m})}{F(100\ \mu{\rm m})} \qquad (1)$$

where the $F(45\ \mu$m), and $F(100\ \mu$m) fluxes are determined from ISO–Long Wavelength Spectrometer (ISO–LWS) spectra. We checked for contamination by extended emission in the 80” ISO–LWS beam, by comparing with the ISO–SWS flux at 45 μm in a 20” beam. For most sources there is good agreement within the instruments cross calibration uncertainty of $\sim$ 30%. An exception is W 3 : IRS5, with a difference of more than a factor of 2, and we consider the flux ratio unreliable. We find that sources with a large narrow $^{13}CO_2$ peak strength have a high hot/cold dust flux ratio (Table 4; Fig. 9). And indeed, sources with low upper limits to the $^{13}CO_2$ substructure, such as W 33A, NGC 7538 : IRS9, and Elias 29, are surrounded by much larger fractions of cold dust.

A similar picture is seen in the gas phase characteristics. Near-infrared CO observations indicate that a large fraction ($\sim$50%) of the gas toward the objects with the narrow $^{13}CO_2$ ice substructure is hot, $T = 400 - 1000$ K (Table 4). It must be noted that in all objects the temperature of the hot CO gas is well above the ice sublimation temperature $T = 90$ K, and thus the observed heated CO_2 ice originates from a region outside the hot core. On the other hand, the temperature of the cold CO gas component is in some lines of sight too low to cause the CO_2 ice to segregate (e.g. $T = 28$ K for S 140 : IRS1; Mitchell et al. 1990). Perhaps the observed hot CO_2 ice originates from the interface between the hot core and the cool surrounding medium. Indeed, other gas phase temperature tracers (e.g. CH_3CN, CH_3OH; van der Tak et al. 1999) reveal temperatures that are in between the cold and hot components found by CO studies.

Finally, the abundance of volatiles, such as ices, is expected to be a good tracer of the dust temperature along the line of sight. Indeed, sources with low CO_2 abundances have the strongest substructure in the $^{13}CO_2$ ice band (Table 4; Fig. 9). For solid CO, a similar trend is observed. The objects with the strongest narrow $^{13}CO_2$ peaks, S 140 : IRS1 and GL 2591, have no detected CO ice along the line of sight. This contrasts with W 33A and NGC 7538 : IRS9, which even have detections of highly volatile apolar CO detections (Smith et al. 1989; Tielens et al. 1991). All low-mass objects have a high fraction of apolar CO, and at the same time show no sign of heated CO_2 ice along the line of sight.

Thus, we find that the strength of the narrow $^{13}CO_2$ component at 2282 cm^{-1} correlates with the dust and CO gas temperature along the line of sight, and anti-correlates with the ice abundances. This is good evidence that the observed feature can be attributed to a heated polar CO_2 ice, and it confirms our results from the laboratory fits. Thermal processing is thus an important process in interstellar space, at least toward luminous protostars. The differences in the various lines of sight are intriguing, and may indicate an evolutionary sequence with increasing thermal processing. Perhaps several distinct layers exist around massive protostars, in a way sketched in Ehrenfreund et al. (1998): a hot core where the ices have evaporated, a warm region surrounding it, where ice crystallizes, and further out a colder region. With time, these temperature regions expand outward. This would correspond to the two component ice model, where the narrow peak and broad components arise in physically different regions (Sect. 4.2.1).

Table 4. Strength of the narrow $^{13}CO_2$ ice peak and observed physical parameters from literature

Object	$\frac{\text{narrow}}{\text{broad}}{}^{13}CO_2{}^a$	$N^b_{\rm hot\ CO}$	$T_{\rm hot\ CO}$	$N^c_{\rm apolar\ CO}$		$L_{\rm bol}$		$F_{\rm hot}/F^d_{\rm cold}$
		%	K	%	ref.	$L_\odot$	ref.	
S 140 : IRS1	1.6 (0.3)	41 (10)	390	0	[4]	$3\ 10^4$	[10]	3.2
GL 2591	1.9 (0.4)	56 (10)	1010	0	[2]	$6\ 10^4$	[10]	4.4
GL 2136	1.0 (0.1)	32 (16)	580	< 10	[3]	$7.2\ 10^4$	[9]	2.8
W 3 : IRS5	1.0 (0.1)	50 (25)	580	80	[3]	$4.7\ 10^5$	[15]	4.1^f
NGC 7538 : IRS9	< 0.7	2 (1.5)	180	92 (11)	[1]	$9.2\ 10^4$	[14]	2.1
Elias 29	< 0.5	—	—	88	[5]	36	[13]	2.0
W 33A	< 0.5	52 (26)	120	26 (3)	[1]	$1.1\ 10^5$	[10]	1.3
Elias 16	< 0.4	—	—	86 (4)	[6]	—	—	—
GC 3	< 0.3	—	—	0	[7]	—	—	—
R CrA : IRS2	< 0.7	—	—	92 (34)	[1]	12	[8]	—
NGC 2024 : IRS2	< 0.9	—	—	74	[3]	$1\ 10^3$	[12]	—
HH 100	< 0.6	—	—	63 (7)	[1]	14	[8]	1.1
GL 989	$—^e$	—	—	71	[3]	$3.3\ 10^3$	[11]	—

[a] narrow over broad Gaussian $^{13}CO_2$ peak depth ratio

[b] hot CO gas column density in percentage of total N(CO gas); Mitchell et al. 1990

[c] column density of CO in apolar ice in percentage of total N(CO ice). Entries with '0' indicate that no CO ice was detected, with a significant upper limit.

[d] calculated as $F(45\mu\text{m})/F(100\mu\text{m})$ from ISO–LWS spectra

[e] line profile unresolved

[f] observed FIR flux heavily contaminated by nearby objects

References: [1] Chiar et al. 1998; [2] van Dishoeck et al. 1996; [3] Tielens et al. 1991; [4] Gerakines et al. 1999; [5] Kerr et al. 1993; [6] Chiar et al. 1995; [7] Schutte et al. 1998; [8] Wilking et al. 1989; [9] Kastner et al. 1994; [10] Gürtler et al. 1991; [11] Henning et al. 1990; [12] Maihara et al. 1990; [13] Chen et al. 1995; [14] Chini et al. 1986; [15] Berrilli et al. 1989

Alternatively, the very good fits that we obtain with single ices, would suggest that all the ice has one specific temperature, and thus is present in a specific region around the protostar. The temperatures of the least (W 33A; T=115 K) and most (S 140; T=118 K) evolved luminous objects are extremely well constrained in an interval of only 3 K. At the long time scales in interstellar space, this small temperature difference can be translated to a difference in heating time at the amorphous-crystalline phase transformation (segregation) temperature. Amorphous ice has a highly disordered structure, characterized by a broad distribution of bond angles between neighboring H_2O molecules (Madden et al. 1978). In contrast, crystalline ice has well defined bond angles. This broad distribution implies a range of activation energies associated with the amorphous-crystalline phase transition. At a relatively low temperature in the laboratory ($T = 115$ K), only the lowest barriers can be surmounted. As the temperature increases (to $T = 118$ K), the higher barriers can be scaled as well. Hence, this temperature range implies a variation in barrier height by about 3%, with a typical height of $E_{\rm segr}$=4600 K (calculated from a 5500 K barrier at 140 K for pure ice; Tielens & Allamandola 1987). In interstellar space, rather than temperature, time is the essential parameter. The time scale $\tau_{\rm segr}$ needed to surmount an energy barrier $E_{\rm segr}$ at temperature T is given by:

$$\tau_{\rm segr} = \nu_0^{-1}\ {\rm e}^{E_{\rm segr}/T} \tag{2}$$

with $\nu_0 = 5\ 10^{13}\ {\rm s}^{-1}$ the O–H bending mode vibration frequency (Tielens & Allamandola 1987). As the protostar is formed, it heats the surrounding molecular cloud, creating a hot core region around it where the ice evaporates. Immediately surrounding this region is a zone where the ice has been warmed sufficiently to start the amorphous- crystalline phase transformation, corresponding to the $T = 115$ K case in the laboratory. As time progresses, this phase transformation progresses as well, and in essence, although the temperature does not change, the interstellar ice corresponds to warmer and warmer (i.e. 115–118 K) laboratory experiments. At the typical time scale of evolution for hot core regions of $\tau \sim 3\ 10^4$ years (Charnley et al. 1992), the laboratory temperature range of 115–118 K effectively corresponds to a segregation temperature of $\sim$77 K (Eq. 2). Thus, at this temperature, W 33A and NGC 7538 : IRS9 would have the youngest and least evolved hot cores, while S 140 and GL 2591 are $\sim 3\ 10^4$ years older and have succeeded to heat the surrounding gas and ice significantly. However, the derivation of a heating time scale is complicated by the presence of temperature gradients, and possible intrinsic differences between the sources. It seems thus likely that both time and temperature effects play a role in the evolution of interstellar CO_2 ices. Detailed modeling of the temperature and density structure around massive protostars is needed to derive evolutionary time scales (e.g. Van der Tak et al. 1999).

5.2. Chemistry of interstellar CO_2

Interstellar CO_2 may form on grain surfaces, through the reaction of atomic O with CO, atomic C, or C^+, accreted from the gas phase. Although CO, rather than C or C^+, is generally assumed to be the origin species, solid and gas phase isotope $^{12}C/^{13}C$ ratios provide a good test for this (Sect. 5.3). In this grain surface scenario, the ice composition provides a measure for the gas phase abundances during accretion, convolved with reaction efficiencies. The ratio of CH_3OH/CO_2 is a measure for hydrogenation over oxidation reactions of CO. The $^{13}CO_2$ profile provides an upper limit $CH_3OH/CO_2 \leq 1$ in the ice, and thus oxidation of CO is at least as efficient as hydrogenation, despite the much larger atomic H abundance compared to atomic O. At the same time, the solid H_2O/CO_2 ratio measures the gas phase $(O+O_2)/CO$ ratio at accretion, since H_2O is formed from O_2 or O_3. The $^{13}CO_2$ profile does not significantly constrain the solid H_2O/CO_2 ratio, it could be as high as the ratio of column densities, i.e. $H_2O/CO_2 \leq 5$ (Gerakines et al. 1999). Further constraints to the chemical conditions during CO_2 formation on interstellar grains can be obtained from the $^{12}CO_2$ bending and stretching modes (Gerakines et al. 1999; Boogert 1999). In particular, the prominent red wing in the bending mode is a signature for the presence of CO_2:CH_3OH clusters in interstellar ices.

An alternative way to form interstellar CO_2 is through irradiation of CO containing ices by ultraviolet (UV) photons. Even in "cold" sight-lines such as Elias 16, the UV flux from the ISRF or induced by cosmic rays may be high enough to explain the observed CO_2 abundance (see Whittet et al. 1998 for a quantitative discussion). The oxygen atoms are liberated from H_2O in polar ices, or O_2 in apolar ices. The interstellar $^{13}CO_2$ profile does not show the narrow signatures of CO_2 mixed with apolar molecules such as CO and O_2. Hence, if UV processing is the dominant mechanism, CO_2 most likely originates from polar CO ices. Indeed, interstellar CO is present in significant quantities in the polar phase (Tielens et al. 1991; Chiar et al. 1998).

5.3. Galactic $^{12}C/^{13}C$ *abundance ratio*

The derived $^{13}CO_2$, and published $^{12}CO_2$, column densities were used to calculate $^{12}C/^{13}C$ abundance ratios (Table 3). It is the first time that the $^{12}C/^{13}C$ ratio is determined from the solid state. Previously, gas phase molecules were used for this purpose, using UV, optical, and radio observations (see Wilson & Rood 1994 for an overview). $C^{18}O$ and H_2CO observations yield an increasing $^{12}C/^{13}C$ ratio with Galacto-centric radius (Langer & Penzias 1990). This can be understood by the different origin of ^{12}C and ^{13}C atoms. The ^{12}C is rapidly produced by Helium burning in massive stars, and injected into the interstellar medium by supernovae. In later stellar generations, ^{12}C seeds are converted to ^{13}C in the CNO cycle of low- and intermediate-mass stars, during their red giant phase. This is a much slower process. Thus, the $^{12}C/^{13}C$ ratio is a measure for the enrichment of the interstellar medium by primary to secondary stellar processes. The observed gradient in the Galactic $^{12}C/^{13}C$ ratio can then be understood by a higher star formation rate in the inner parts of the Galaxy (Tosi 1982).

The $^{12}C/^{13}C$ ratio derived from solid CO_2 indicate the same trend as found in gas phase studies (Table 3; Fig. 10). Low values are found near the Galactic Center ($^{12}CO_2/^{13}CO_2$=52±11; GC 3) and in the molecular ring, at ∼4 kpc from the Galactic Center (W 33A; 53±8). Objects at larger Galactic radii mostly have higher $^{12}CO_2/^{13}CO_2$ ratios. We have fitted a linear relation to the $^{12}CO_2/^{13}CO_2$ ratio as a function of Galacto-centric radius, where, as in the gas phase studies, we exclude the Galactic Center from the fit. We find the following relation, using the errors as statistical weights:

$$(^{12}CO_2/^{13}CO_2) = (4.5 \pm 2.2)R_G + (48 \pm 16) \qquad (3)$$

If instead we take an unweighted fit, like in some gas phase studies (Wilson & Rood 1994), we find a gradient of 6.5±4.5 and absisca 33±21. Thus, the evidence for a gradient in the $^{12}C/^{13}C$ ratio derived from solid CO_2 is weak. Within the (rather large) error bars, this gradient is comparable to the H_2CO (6.6±2.0) and CO data (7.5±1.2). It must be mentioned that a limitation of our analysis is the lack of solid CO_2 observations at low Galactic radii (3–6 kpc). We note that also in gas phase studies (Wilson & Rood 1994), there is considerable scatter in the $^{12}C/^{13}C$ ratio, and no clear trend at Galactic radii > 6 kpc is present either (Fig. 10).

Although the gradients agree well for CO_2, CO, and H_2CO, we find that $^{12}C/^{13}C$ ratios derived from CO (abscissa −2.9±7.5 in Eq. 2) are systematically somewhat smaller. A comparison of the gas and solid state $^{12}C/^{13}C$ ratios for individual objects is possible for only 4 sources. For all of these, our solid CO_2 observations yield higher $^{12}C/^{13}C$ ratios compared to gas phase CO observations (Table 3). However, for both the overall linear fit (Eq. 2) and for these individual sources, the differences are statistically small ($< 3\sigma$). For a proper interpretation of these possible differences it is important to note that the gas phase observations were done several arcminutes away from our CO_2 observations (Table 3). In the gas phase, considerable variations of the $^{12}C/^{13}C$ ratio were reported within the same region, such as within the W 33 cloud

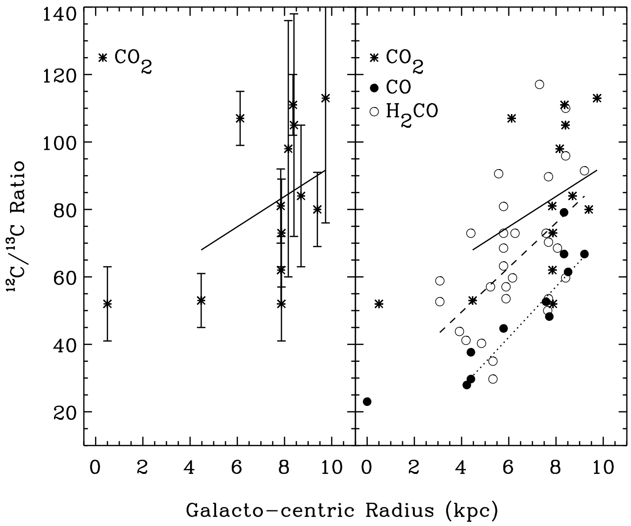

Fig. 10. The ratio of solid $^{13}CO_2$ and $^{12}CO_2$ column densities, versus the Galacto-centric radius of the observed sources (left panel). The solid line is a linear weighted fit to the data. The right panel shows the $^{12}C/^{13}C$ ratio from gas phase studies (bullets: $C^{18}O$, open circles: H_2CO) as taken from Wilson & Rood (1994). The dotted and dashed lines are linear fits to these gas data.

(Langer & Penzias 1990) and toward the supernova remnant Cas A (Wilson & Rood 1994). In particular, comparison of our $^{12}CO_2/^{13}CO_2$ ratio toward the Galactic Center object GC 3 with the gas phase determination toward the Galactic Center supernova remnant Sgr B2 is complicated by the quite different stellar evolution history that these regions may have.

Finally, we determined that $^{12}CO_2/^{13}CO_2$=69±15 (1 σ) for the local ISM, by taking an unweighted mean for the three objects located in the ρ Ophiuchi, and Corona Australis clouds. We excluded Elias 16 from this mean, since it has a much larger error bar than the other sources (Table 3). This value is comparable to the $^{12}C/^{13}C$ ratio in the local ISM, as determined from atomic C (58±12; Keene et al. 1998) and C^+ (58±6; Boreiko & Betz 1996) observations, as well as from $C^{18}O$ and H_2CO observations ($^{12}C/\ ^{13}C$=77±7; Wilson & Rood 1994).

In summary, we find that the gradient of the $^{12}C/^{13}C$ ratio with Galacto-centric radius is the same for solid CO_2 and gaseous CO and H_2CO. In this relation, the values derived from CO, however, tend to be smaller compared to CO_2 and H_2CO. The value for the local ISM ($^{12}CO_2/^{13}CO_2$= 69±15) is in reasonable agreement with gas phase studies. These results could have important implications for our knowledge of interstellar chemistry. Both gaseous CO and H_2CO may have been affected by chemical fractionation and isotope selective destruction (e.g. Langer et al. 1984; Tielens 1997). If fractionation is an important mechanism, preferential incorporation of $^{13}C^+$ in CO, leads to low $^{12}CO/^{13}CO$ and high $^{12}C^+/^{13}C^+$ ratios. On the other hand, if isotope selective destruction dominates over fractionation, ^{13}CO is preferentially destroyed, leading to high $^{12}CO/^{13}CO$ and low $^{12}C/^{13}C$ ratios. Carbonaceous molecules derived from C^+ or C would then have high or low $^{12}C/^{13}C$ ratios, depending on the dominant process and chemical pathway. Our lines of sight trace dense molecular clouds, and CO is the main reservoir of C. Then, fractionation or selective destruction will highly influence the $^{12}C^{(+)}/^{13}C^{(+)}$ ratio, but will hardly affect the $^{12}CO/^{13}CO$ ratio. The generally higher $H_2^{12}CO/H_2^{13}CO$ ratios compared to CO thus suggest that H_2CO originates from C^+ (Tielens 1997). Similarly, if indeed the $^{12}CO_2/^{13}CO_2$ ratios are higher compared to CO, this would imply that CO_2 is formed from C^+ rather than C or, as is generally assumed, from CO (van Dishoeck et al. 1996). However, we must emphasize that with the present large uncertainties in the $^{12}C/^{13}C$ ratios we can not make strong statements about the chemical pathway to form interstellar CO_2. We expect that with future improvements of the ISO–SWS data reduction, the large error bars in the CO_2 abundances for some sources (GL 989, NGC 2024 : IRS2, and W 3 : IRS5) can be reduced. Furthermore, it is important to obtain $^{12}CO/^{13}CO$ ratios in the same line of sight as our CO_2 observations, preferably by absorption line studies along a pencil beam. Observations of the solid $^{12}CO/^{13}CO$ ratio would be particularly useful. This will also shed light on the origin of the large scatter seen in the $^{12}C/^{13}C$ ratio as a function of Galacto-centric radius for both solid CO_2 (i.e. note the particularly high value for GL 2136 in Fig. 10) and gas phase species. It has been suggested that perhaps most of this scatter is real, and can be attributed to local variations in the star formation history (Wilson & Rood 1994).

6. Summary and Conclusions

We have presented ISO–SWS observations of the stretching mode of $^{13}CO_2$ ice in the spectral range 2255–2300 cm^{-1} (4.34–4.43 μm) in 13 Galactic lines of sight. All sight-lines show an absorption feature with a peak position in the range 2276–2280 cm^{-1}, and a Gaussian FWHM of typically 6-9 cm^{-1}. Additionally, the four high-mass protostars GL 2136, S 140 : IRS1, GL 2591, and W 3 : IRS5, show a narrow (FWHM∼3 cm^{-1}) absorption line at ∼ 2282.3 cm^{-1}. This feature is much weaker or absent toward other high-mass objects (W 33A, NGC 7538 : IRS9), toward low-mass protostars, the Galactic Center (GC 3), and quiescent molecular cloud material (Elias 16).

These observational results are compared to laboratory experiments of the stretching mode of $^{13}CO_2$ ice. We conclude that this band is a sensitive probe of the heating history and composition of interstellar ice mantles. The profile of the interstellar band can be fitted in two different ways. First, the detected broad and narrow components could originate from ices with different heating histories and perhaps composition along the line of sight.

In this scenario, the detected broad component is ascribed to a non-heated mixture of CO_2 with polar molecules such as most likely H_2O, and CH_3OH. The mixing ratio of CH_3OH/CO_2 in the ice can generally be constrained to an upper limit of $CH_3OH/CO_2 \leq 1$, in agreement with the observed column densities along the lines of sight. The narrow 2282 cm^{-1} absorption feature detected toward several high-mass protostars is ascribed to $^{13}CO_2$ in a polar CO_2 ice that has been heated to temperatures of at least 50 K (in interstellar space). In such an ice, the bondings of the CO_2, and polar molecules are segregated and the CO_2 band profiles resemble those in a pure CO_2 ice. To fit the exact peak position of the 2282 cm^{-1} feature, the CO_2 ice must contain at least some CH_3OH ($CH_3OH/CO_2 > 0.1$).

A second way to fit the $^{13}CO_2$ band, is with a single ice at a specific temperature. This would locate the ice in a well confined region around the protostar, rather than in regions of different temperature as for the two component model. For the luminous protostars showing evidence for this narrow component, the best fitting laboratory ices have temperatures within a very small interval of $T = 115 - 118$ K (using H_2O:CH_3OH:CO_2=1:1:1). At the long time scales in interstellar space, this laboratory temperature interval corresponds to a heating time difference between the luminous protostars comparable to the lifetime of hot cores ($\sim 3\ 10^4$ years) at an amorphous-crystalline phase transition temperature of ~77 K. However, the derivation of heating time scales likely is complicated by the presence of temperature gradients, and possible intrinsic differences between the sources, such as different temperature and density structure.

To further test the hypothesis that interstellar CO_2 ice is affected by heating, we calculate the ratio, and upper limits, of the narrow to broad $^{13}CO_2$ component peak depths. This quantity is compared to known physical parameters of all objects. We conclude that the strength of the narrow $^{13}CO_2$ substructure correlates with the dust and CO gas temperature along the line of sight, and anti-correlates with the ice abundances. This is further good evidence that the structure of ices around luminous protostars is affected by thermal processing, as concluded from the laboratory fits. This effect appears to be not important for low mass protostars and the quiescent medium. Although we have to keep in mind that our selection of low mass objects is small, this might imply that unaltered interstellar ices are included in comets.

Finally, we have determined solid $^{13}CO_2$ column densities. These were used to derive $^{12}C/^{13}C$ ratios in all 13 sight-lines. It is the first time that the Galactic $^{12}C/^{13}C$ ratio is determined from the solid state. Solid state determinations of the $^{12}C/^{13}C$ ratio are more reliable than gas phase studies, because the column density can be determined without uncertain radiative transfer effects. Like in gas phase studies, we find low values for the Galactic Center (GC 3; $^{12}CO_2/^{13}CO_2 = 52 \pm 11$) and the Galactic molecular ring (W 33A; 53±8), and higher values at larger Galacto-centric radii. The gradient of the $^{12}CO_2/^{13}CO_2$ ratio as a function of Galacto-centric radius (4.5 ± 2.2 kpc^{-1}) agrees with gas phase studies. The scatter in this relation is however large, and may perhaps indicate local differences in star formation history, since ^{12}C is converted to ^{13}C in low and intermediate mass stars. Comparison of solid and gas phase isotope ratios can be used to trace the chemical history of molecules. In general, the $^{12}CO_2/^{13}CO_2$ ratio, as for H_2CO, tends to be larger compared to CO studies ($\sim 2.5\ \sigma$ difference). In the dense molecular clouds that we have observed, where CO is likely unaffected by fractionation or isotope-selective destruction, this would imply that interstellar CO_2 is formed from C^+, rather than CO or C. However, to draw definite conclusions on interstellar chemistry and on global and local variations in the Galactic star formation history, we emphasize that a systematic determination of the $^{12}C/^{13}C$ ratio from atomic $C^{(+)}$, CO, and solid CO_2 in individual lines of sight is needed. At present, there is little overlap between our solid CO_2 observations and published gas phase observations.

Acknowledgements. We thank the ISO–SWS instrument dedicated teams of Vilspa (Madrid, E), SRON (Groningen, NL), and KUL (Leuven, B) for help in the data reduction at many stages during this research. We thank I. Yamamura for suggestions on correcting for the photospheric lines in Elias 16, and F. van der Tak for discussing temperature and evolution indicators in high mass protostars. L.D. is supported by the Fund for Scientific Research of Flanders. D.C.B.W. is funded by NASA through JPL contract no.961624 (ISO data analysis) and by the NASA Exobiology and Long-Term Space Astrophysics programs (grants NAG5-7598 and NAG5-7884). This research has made use of the Simbad database, operated at CDS, Strasbourg, France.

References

Aitken D.K., Wright C.M., Smith C.H., Roche P.F., 1993, MNRAS 262, 456

Allamandola L.J., Sandford S.A., Tielens A.G.G.M., Herbst T.M., 1992, ApJ 399, 134

Berrilli F., Ceccarelli C., Liseau R., et al., 1989, MNRAS 237, 1

Blake D., Allamandola L., Sandford S., Hudgins D., Freund F., 1991, Sci 254, 548

Boogert A.C.A., 1999, Ph. D. thesis, University of Groningen

Boreiko R.T., Betz A.L., 1996, ApJ 467, L113

Charnley S.B., Tielens A.G.G.M., Millar T.J., 1992, ApJ 399, L71

Chen H., Myers P.C., Ladd E.F., Wood D.O.S., 1995, ApJ 445, 377

Chernin L.M., 1996, ApJ 460,711

Chiar J.E., Adamson A.J., Kerr T.H., Whittet D.C.B., 1995, ApJ 455, 234

Chiar J.E., Adamson A.J., Whittet D.C.B., 1996, ApJ 472, 665

Chiar J.E., Gerakines P.A., Whittet D.C.B., et al., 1998, ApJ 498, 716

Chini R., Krügel E., Kreysa E., 1986, A&A 167, 315 de Graauw Th., Haser L.N., Beintema D.A., et al., 1996, A&A 315, L49

d'Hendecourt L.B., Jourdain de Muizon M., 1989, A&A 223, L5

d'Hendecourt L.B., Jourdain de Muizon M., Dartois E., et al., 1996, A&A 315, L365

Ehrenfreund P., Boogert A.C.A., Gerakines P.A., et al., 1996, A&A 315, L341

Ehrenfreund P., Boogert A.C.A., Gerakines P.A., Tielens A.G.G.M., van Dishoeck E.F., 1997, A&A 328, 649

Ehrenfreund P., Dartois E., Demyk K., d'Hendecourt L., 1998, A&A 339, L17

Ehrenfreund P., Kerkhof O., Schutte W.A., et al., 1999, A&A, in press

Elias J.H., 1978, ApJ 224, 857

Gerakines P.A., Schutte W.A., Greenberg J.M., van Dishoeck E.F., 1995, A&A 296, 810

Gerakines P.A., Whittet D.C.B., Ehrenfreund P., et al., 1999, ApJ 522, 357

Goorvitch D., 1994, ApJS 95, 535

Gürtler J., Henning Th., Krügel E., Chini R., 1991, A&A 252, 801

Gürtler J., Henning Th., Kömpe C., et al., 1996, A&A 315, L189

Henning Th., Pfau W., Altenhoff W.J., 1990, A&A 227, 542

Kastner J.H., Weintraub D.A., Snell R.L., 1994, ApJ 425, 695

Keene J., Schilke P., Kooi J., et al., 1998, ApJ 494, L107

Kerr T.H., Adamson A.J., Whittet D.C.B., 1993, MNRAS 262, 1047

Kessler M.F., Steinz J.A., Anderegg M.E., et al., 1996, A&A 315, L27

Langer W.D., Graedel T.E., Frerking M.A., Armentrout P.B., 1984, ApJ 277, 581

Langer W.D., Penzias A.A., 1990, ApJ 357, 477

Madden W.G., Bergren M.S., McGraw W.R., Rice S.A., 1978, J.Chem.Phys. 69, 3497

Maihara T., Mizutani K., Suto H., 1990, ApJ 354, 549

Mitchell G.F., Maillard J.-P., Allen M., Beer R., Belcourt K., 1990, ApJ 363, 554

Mitchell G.F., Maillard J.-P., Hasegawa T.I., 1991, ApJ 371, 342

Okuda H., Shibai H., Nakagawa T., et al., 1990, ApJ 351, 890

Rothman L.S., Gamache R.R., Tipping R.H., et al., 1992, J. Quant. Spectrosc. Radiat. Transfer 48, 469

Sandford S.A., Allamandola L.J., 1990, ApJ 355, 357

Saraceno P., André P., Ceccarelli C., Griffin M., Molinari S., 1996, A&A 309, 827

Schutte W.A., van der Hucht K.A., Whittet D.C.B., et al., 1998, A&A 337, 261

Smith R.G., Sellgren K., Tokunaga A.T., 1989, ApJ 344, 413

Strazzulla G., Nisini B., Leto G., Palumbo M.E., Saraceno P., 1998, A&A 334, 1056

Tielens A.G.G.M., 1997, Deuterium and interstellar chemical processes. In: Bernatowicz Th.J., Zinner E. (eds.) Astrophysical implications of the laboratory study of presolar materials. AIP, Woodbury NY, p. 523

Tielens A.G.G.M., Allamandola L.J., 1987, Composition, structure, and chemistry of interstellar dust. In: Hollenbach D.J., Thronson Jr. H.A. (eds.) Interstellar Processes. Reidel, Dordrecht, p. 414

Tielens A.G.G.M., Tokunaga A.T., Geballe T.R., Baas F. , 1991, ApJ 381, 181

Tosi M., 1982, ApJ 254, 699

Valentijn E.A., Feuchtgruber H., Kester D.J.M., et al., 1996, A&A 315, L60

van der Tak F., van Dishoeck E.F., Evans II N.J., Bakker E.J., Blake G.A., 1999, ApJ 522, 991

van Dishoeck E.F., Helmich F.P., de Graauw Th., et al., 1996, A&A 315, L349

Whittet D.C.B., 1974, MNRAS 168, 371

Whittet D.C.B., Gerakines P.A., Tielens A.G.G.M., et al., 1998, ApJ 498, L159

Wilking B.A., Lada C.J., Young E.T., 1989, ApJ 340, 823

Wilson T.L., Rood R.T., 1994, ARA&A 32, 191